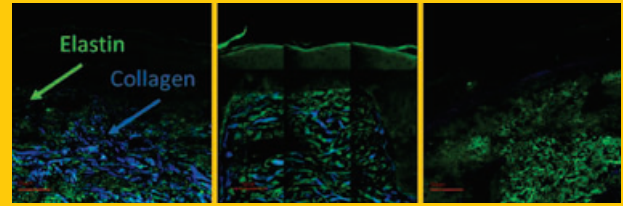


Abstract In this review, the authors discuss the underlying principles of SHG and specific factors that affect the generation properties and describe the essential components of a SHG instrument. In addition, results on the recent progress and impact SHG microscopy has made in different areas of biology and medicine are presented. In particular, the authors focus on disease diagnosis and basic research associated with connected tissues, musculo-skeletal disorders, and epithelial cancers. The presentation is concluded by offering a perspective on the future technical development of SHG microscopy and additional forefronts to be addressed.



SHG and multiphoton autofluorescence imaging of ex-vivo human dermis in 20 (left), 40 (middle), and 70 (right) years-old patients, where blue = SHG and green = autofluorescence.

Second harmonic generation microscopy: principles and applications to disease diagnosis

Paul J. Campagnola^{1,*} and Chen-Yuan Dong^{2,*}

1. Introduction

In the last several years, Second Harmonic Generation (SHG) has emerged as a powerful nonlinear optical contrast mechanism for biological and biophysical imaging applications. SHG is a coherent process where two lower energy photons are up-converted to exactly twice the incident frequency (or half the wavelength). Biological SHG imaging was first reported in 1986 when Freund and coworkers used this contrast mechanism to investigate the polarity of collagen fibers in rat tail tendon [1]. While this work was performed at low resolution (~ 50 microns), it together with an earlier demonstration of SHG microscopy [2], showed initial proof of concept that, in part, laid the foundation for modern versions of SHG imaging. The evolution into a viable tool has been enabled by technology developments in suitable off-the-shelf, modelocked, ultrafast lasers along with the development of laser scanning and data acquisition hardware/software. These enhancements have similarly rendered the advancement of multiphoton excited fluorescence microscopy into a routine imaging scheme.

An explosion of research in the past decade has shown the promise of SHG in tissue imaging. The majority of the recent reports have focused on visualizing collagen fibers in a variety of connective tissues including skin, bone, tendon, blood vessels, and cornea as well as fibrotic collagen in internal organs such as lung, liver, and kidney [3–18]. In addition, the fibrillar structure of self-assembled or reconstituted collagen structures has also been investigated [19, 20]. A smaller body of publications has described SHG imaging of acto-myosin complexes in muscle as well as microtubule-based structures in live cells [21–24]. By now the anatomical

landscape of SHG sources has been quite well explored, and the conclusion is that type I and II collagen, as well as myosin (within actomyosin complexes) are the predominant harmonophores producing imageable rates of SHG in tissue. In contrast, random molecular assemblies formed by elastin (e.g. in dermis) do not produce measurable SHG.

In addition to identifying the predominant harmonophores that provide sufficient contrast for imaging, crucial biochemical and structural considerations have also been identified. For example, the genetic, biochemical and biophysical experiments probing the origin of SHG in myofibrils are consistent with the contrast arising from the myosin tail domain [21, 25]. However, other work has pointed to contributions from the myosin head [24], pointing to the need for more work in this area. Other parallel efforts have focused on elucidating the physical principles that give rise to SHG in tissues in terms of the coherence and polarization properties and how they relate to the fibrillar organization [22, 25, 26].

SHG has several advantageous features that make it an ideal approach for imaging tissues *in situ*. A particularly strong attribute of the SHG method lies in the property that, in tissues, the contrast is produced purely from endogenous species. This coupled with the physical basis that the SHG signals arise from an induced polarization rather from absorption leads to substantially reduced photobleaching and phototoxicity relative to fluorescence methods (including multiphoton). In addition, as laser fundamental wavelengths are in the near infrared spectral range, high resolution, deep tissue imaging to depths of several hundred microns can be readily achieved [21]. Perhaps the most important and unique feature to this contrast mechanism is the sensitivity

¹ Department of Cell Biology, Center for Cell Analysis and Modeling, University of Connecticut Health Center, Farmington, CT 06030, USA ² Department of Physics and Center for Quantum Science and Engineering, National Taiwan University, Taipei 106, Taiwan
* Corresponding authors: e-mail: campagno@neuron.uchc.edu, cydong@phys.ntu.edu.tw

of the SHG signatures to physical structure (described in detail in Sect. 2).

The efforts over the past decade have established SHG as a viable imaging technique and real-life applications are emerging, especially as a diagnostic tool for diseases and other pathological conditions. Due to the exquisite sensitivity of SHG to supramolecular structure, there is considerable optimism that SHG imaging may be translated to clinical applications supplementing classical histological methods of pathologists. In this review, we present a summary of current research in this framework by showing how SHG has been used in the imaging of connective tissue disorders, musculoskeletal diseases, organ fibrosis, cardiovascular pathologies, and cancers. We first begin with an overview of the physical origin of SHG in fibrillar tissues follow by discussion of experimental considerations. Next, we will review current literature on disease applications, and conclude with perspectives for eventual translation to the clinic.

2. Physical description

2.1. Nonlinear response

In general, the total polarization for a material can be expressed as:

$$P_i = \chi_{ij}^{(1)} E_j + \chi_{ijk}^{(2)} E_j E_k + \chi_{ijkl}^{(3)} E_j E_k E_l + \dots \quad (1)$$

where P is the induced polarization, $\chi^{(n)}$ is the n th order non-linear susceptibility tensor, and E is the electric field vector. The second order nature of SHG imposes severe symmetry restrictions on the harmonophores and their assembly that can be imaged, as the environment must be non-centrosymmetric on the size scale of λ_{SHG} . The nonlinear susceptibility tensor, $\chi^{(2)}$ is a bulk property and is the quantity measured in an experiment. However, the molecular level property of the nonlinearity, i.e. the first hyperpolarizability, β , needs to be considered as it forms the basis of the contrasting mechanism. This parameter is defined in terms of the permanent dipole moment:

$$d^{(2)} = \beta EE \quad (2)$$

The molecular and bulk properties are then related by:

$$\chi^{(2)} = N_s \langle \beta \rangle \quad (3)$$

where N_s is the density of molecules and the brackets denotes their orientational average, which further underscores the need for an environment lacking a center of symmetry. In a two-level description, β is proportional to the permanent dipole moment. In addition, these dipole moments must then be aligned in a non-random fashion to satisfy the bulk property constraints, such that $\chi^{(2)}$ is non-vanishing (Eq. (3)). Thus maximum SHG contrast will be observed for well-aligned molecules that assembly into fibrils. SHG therefore can be used as a direct sensor of supramolecular structure

as deviations from ideal alignment will be manifested in decreased $\chi^{(2)}$ values and other signatures described below. For example, Campagnola and coworkers showed that the relative SHG conversion efficiency in tissues from the mouse model of osteogenesis imperfecta, OI, which is characterized by abnormal collagen assembly, was 3 fold smaller compared to the normal tissue [27].

2.2. Key attributes of SHG

Developing a thorough description of the SHG creation physics in biological tissues is an essential step for this imaging modality to become a useful clinical diagnostic tool for monitoring disease severity and progression. Here we characterize the generation physics by defining the creation attributes as the SHG emission directionality and the conversion efficiency in terms of the relative $\chi^{(2)}$ values. SHG from fibrillar tissues is a different process from that in the more familiar environments of uniaxial doubling crystals and interfaces. In the former case, SHG is perfectly phase matched, i.e. $\Delta \mathbf{k} = \mathbf{k}_{2\omega} - 2\mathbf{k}_\omega = 0$, where $\mathbf{k}_{2\omega}$ is the wave vector for SHG photon and \mathbf{k}_ω is the wave vector for the incident photon. SHG from interfaces, including that from dye labeled membranes is also phase matched. The SHG emission from these perfectly phase matched systems is 100% forward directed, however the SHG from tissues never completely satisfies this condition and a result the emission is characterized by a distribution of forward and backward components. As discussed below, this can be useful for differentiating normal and diseased tissues.

Several reports have discussed the SHG emission directionality in fibrillar tissues, where arguments based on size of the fibrils are used to explain the observed distribution. For example, Han and Webb reported the emission directionality from collagen fibrils in cornea and rat tail tendon, respectively [6, 12]. Han suggested that the amplitude of the second harmonic field $\mathbf{E}_{2\omega}$ from an ensemble of collagen fibrils was related to a random distribution of dipoles, and that regularly packed lattices would support destructive interferences in all directions except for the transmission direction. Webb made directional comparisons and explained the observations based on the morphological differences in fibril diameter in immature and mature tendons. Previously using antenna theory, Mertz demonstrated that spatial inhomogeneities (axially periodic and spherically localized distributions) are capable of contributing momentum to the phase matching condition and, under appropriate conditions, can account for the creation of backward SHG [28].

To describe the SHG creation process in fibrillar collagen Campagnola and co-workers presented a more general formalism that includes quasi-phase matching (QPM) and additional phase mis-match due to dispersion and randomness all of which lead to the creation of partially-coherent SHG in both the forward and backward directions [26]. QPM allows the buildup of SHG intensity between anisotropic domains (here either single fibrils or assembly of small fibrils) without the need for strict phase

matching conditions (i.e. $\Delta\mathbf{k} \neq 0$). This description is appropriate for the case of medium NA (\sim e.g. 0.8) long working distance objectives where the upper bound of the material coherence length is the same or slightly less than axial PSF (i.e. several microns), where the plane wave approximation is valid.

Unlike birefringent crystals with $\Delta\mathbf{k} = 0$, the axial momentum contributions from the media that are non-singular due to inherent randomness and dispersion inherent in biological tissues result in a large distribution of $\Delta\mathbf{k}$ values. Thus, in biological tissues, the minimum phase mismatch is governed by dispersion in the refractive index between the fundamental and SHG wavelengths and is denoted by $\Delta\mathbf{k}_1$ and the resulting maximum coherence length is $L_c = 2\pi/\Delta\mathbf{k}_1$. The normalized conversion scales as $\sin(m\Delta\mathbf{k}L/2)$, where m is an integer, and is therefore domain length dependant, reaching its first maximum at the respective L_c . Fields associated with larger $\Delta\mathbf{k}$ values will thus be characterized by less-efficient SHG conversion at its maximum value. To place this in context in terms of disease imaging, Campagnola and coworkers showed that larger $\Delta\mathbf{k}$ values (and weaker SHG intensities) were associated with the more disordered skin from the osteogenesis imperfecta mouse model relative to the wild type (WT) [26].

This phase mismatch also has implications for the SHG emission directionality. Due to the fibrillar hierarchy of collagen (often described as a polycrystalline lattice) and measured dispersion ($\Delta n = n(2\omega) - n(\omega) = 0.02$), we assume that $\Delta\mathbf{k}$ values will exist such that the coherence length of the created SHG is on the order of the inter-fibrillar spacing thus allowing for the possibility of QPM. We can then write the following relaxed phase conditions for fibrillar tissues:

$$\Delta\mathbf{k}_f = \mathbf{k}_f - (\mathbf{k}_{2\omega} - 2\mathbf{k}_\omega) \quad (4)$$

and

$$\Delta\mathbf{k}_b = \mathbf{k}_b - (\mathbf{k}_{2\omega} + 2\mathbf{k}_\omega) \quad (5)$$

where $\Delta\mathbf{k}_f$ and $\Delta\mathbf{k}_b$ are the respective phase mismatches for the forward (F_{SHG}) and backward (B_{SHG}) SHG creation. Furthermore, \mathbf{k}_b and \mathbf{k}_f are the axial momentum contributions of the tissue lattice to the backward and forward SHG creation, respectively. Backward SHG creation implies that $\mathbf{k}_b > \mathbf{k}_f$ ($\Delta\mathbf{k}_b > \Delta\mathbf{k}_f$) and results in a distribution of “lower” efficiency SHG components making up the overall B_{SHG} . Consequently, shorter coherence lengths are associated with this component. Thus the SHG conversion efficiency and emission directionality are both related to the phase mismatch that arises from the assembly of the lattice.

Based on this framework, it can be concluded that the SHG creation attributes (conversion efficiency, emission directionality) cannot be adequately described by fibril size alone, and that the fibril diameter, the inter-fibril spacing as well as the randomness of the packing structure must be considered. The coherence lengths of F_{SHG} and B_{SHG} also have implications in the observed fibrillar morphology. For example, in several reports, segmented fibrils have been observed exclusively in the backward channel, while these same fibrils appear to be continuous in the forward

direction [6, 29]. These observations can be explained by differences in coherence lengths using the framework described above.

2.3. Measured directionality

In a tissue imaging experiment, the measured SHG signal will be comprised of a convolution of the quasi-coherent components and their respective directionality (described above) as well as incoherent scattered components [27, 29]. For the scattered component, the depth dependence of the ratio of the forward to backward intensities will be governed by the bulk optical parameters of the matrix at the second harmonic wavelength (i.e. the scattering coefficient, μ_s , and scattering anisotropy, g). In highly scattering tissues this latter contribution will become significant at SHG depths exceeding one mean free path (MFP) or $\sim 1/\mu_s$ of the matrix. For example, using a prototypical fibrillar system (cellulose) Campagnola determined the relative contributions of the directional components in terms of morphology and polarization, and showed how these evolve upon focusing through several hundred microns of tissue (i.e. several scattering lengths) [29].

Differentiating the quasicohherent and incoherent components is an important consideration for clinical applications as diseased states may have smaller and more randomly packed fibrils which affect the initial generation directionality. Such tissues may also have different bulk optical parameters, governing the subsequent photon propagation [27]. Specifically the scattering coefficient and anisotropy generally arise from the tissue density and tissue organization, respectively. As the emitted and scattered photons are experimentally indistinguishable, Monte Carlo techniques must be utilized to describe the effects of propagation through turbid media. Recently the Campagnola lab has reported this approach for imaging osteogenesis imperfecta tissues as well as analyzing results obtained in optical clearing experiments [27, 30].

2.4. Polarization analysis and chiral contributions

In addition to the creation attributes described above, detailed information about the organization of the fibrillar assembly can be extracted from SHG imaging data. This is because the SHG signals have well-defined polarizations with respect to the laser polarization and specimen orientation which can then be used to determine the absolute orientation of the protein molecules in the tissue, as well as the degree of organization of proteins in tissues. These are related to the non-vanishing matrix elements of the 27 component χ^2 tensor. Campagnola has previously shown how the SHG intensity as a function of laser polarization is related to the pitch angle of the protein helix and that the SHG signal anisotropy is related to the dipole assembly [21, 25]. Moreover, deviations from the normal polarization response may indicate the degree of disorganization of

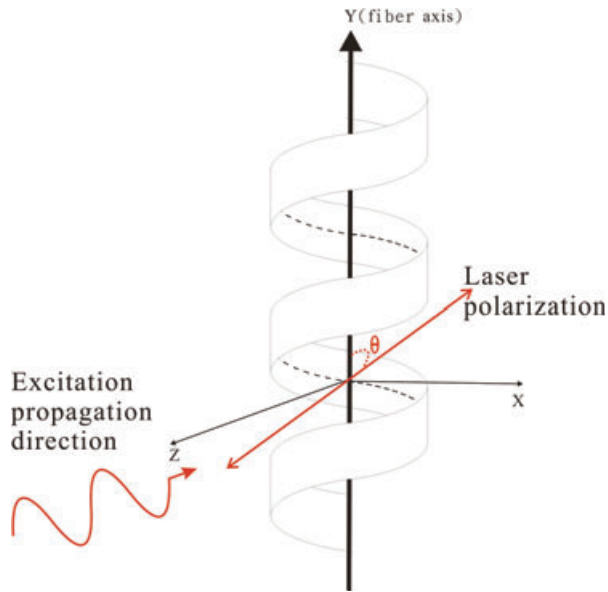


Figure 1 (online color at: www.lpr-journal.org) Relationship between the orientation of the excitation propagation direction (Z-axis), polarization (in X-Y plane), and long axis of the fibrous cylinder (Y-axis). θ is the angle between the long axis of the fibrous cylinder and excitation polarization.

protein structures in diseased tissues [31]. Therefore, polarization analysis offers additional potential for SHG imaging including both the dependence of SHG intensity on the polarization of the laser excitation and polarization anisotropy of SHG signal.

It is well-documented that chirality leads to an enhancement of the second order SHG response [32–34]. Normally folded proteins have inherent chirality due to the helical structure, and as a consequence, this metric may be a diagnostic indicator of diseases that are characterized by a disrupted protein structure. For example, the triple helix in OI collagen may display different chiral contributions in the $\chi^{(2)}$ tensor due to the differences in primary and secondary structure that results from the glycine point mutations. As steps in this direction, several investigators have examined the chiral contributions to the SHG signal in different fibrillar tissues. As shown in Fig. 1, these assemblies have been modeled as cylinders with C_∞ symmetry [22, 25]. Although chirality cannot not be uniquely expressed as single matrix elements of the $\chi^{(2)}$ tensor under this symmetry group, it has been shown for several symmetry groups how the contribution can be written as a sum of the remaining non-vanishing elements. If the laser is propagating in the z direction, then the total SHG intensity can be written as

$$I_{\text{total}}(\theta) \approx I \left[(\rho_1 \cos^2 \theta + \sin^2 \theta)^2 + (\rho_2 \sin^2(2\theta)) \right] \quad (6)$$

where θ is the angle between the laser polarization and the long axis of the cylinder (Y axis) and $\rho_1 = \chi_{yyx}^{(2)}/\chi_{yx}^{(2)}$ and $\rho_2 = \chi_{xyx}^{(2)}/\chi_{yx}^{(2)}$. As described by Cheng [35], $\chi_{xyx}^{(2)}$ and $\chi_{yx}^{(2)}$ are related to the chiral contribution of SHG in the fibrils as these matrix elements lack inversion symmetry. The inten-

sities parallel ($I_Y(\theta)$) or perpendicular ($I_X(\theta)$) polarized to the fibril axis are then given by

$$\begin{aligned} I_Y(\theta) &\approx I(\rho_1 \cos^2 \theta + \sin^2 \theta)^2 \quad \text{and} \\ I_X(\theta) &\approx I(\rho_2 \sin^2(2\theta)). \end{aligned} \quad (7)$$

The parallel and perpendicular components can be measured by rotating the laser polarization and measuring the SHG intensity with a Glan-Laser analyzer parallel or perpendicular to the fiber axis respectively. The total SHG is the sum obtained with no analyzer present. Fitting the experimental data to these expressions then allows the determination of ρ_1 and ρ_2 . Through this type of analysis, Chu et al. found ρ_1 of ~ 0.1 in acto-myosin filaments, indicating a high degree of chirality [22]. In contrast, in astroglial filaments in spinal tissue, Cheng reported ρ_1 of ~ 2.1 , suggesting little chiral contribution [35]. Using sum frequency generation microscopy with polarization analysis Knoesen et al. isolated the molecular aspects of the chiral and achiral components in tendon, where each were similar in their respective contributions [36]. Their assignment of the chiral component to a stretching vibration of the carbonyl groups associated with the amide I band was consistent with the polarization analysis by Plotnikov et al. ascribing the SHG to the helical pitch angle [25]. Similarly, through the use of surface SHG polarization analysis from type I collagen films, Schanne-Klein and coworkers showed the chiral components increased the SHG response by 2 fold [37].

2.5. Applicability to diseases

Collectively, the unique attributes of SHG microscopy described in the previous sections render this method as a promising imaging modality for disease diagnostics in the clinic. In addition, SHG microscopy can be used to reveal details of macromolecular and supramolecular assemblies not possible through techniques such as fluorescence imaging. As we will show in Sect. 4, many diseases are characterized by abnormal fibrillar assembly. In addition, due to the fact the excitation wavelength typically uses near infrared wavelengths (800–1000 nm) produced by titanium-sapphire lasers, this method is well-suited for studying intact tissue samples since excellent depths of penetration can be obtained. For example, Campagnola acquired optical sections into 550 microns of mouse muscle tissue with high contrast throughout the entire axial profile [21]. These depths are governed by the mean free path of tissues, which in the NIR are on the order of 20–50 microns. Thus, about 10 scattering events occur within the achievable depths. In this quasi-ballistic regime, the image resolution is not significantly degraded.

3. Key components of a SHG microscope

Most SHG microscopes described in the literature are constructed by modification of laser-scanning microscopes. Sev-

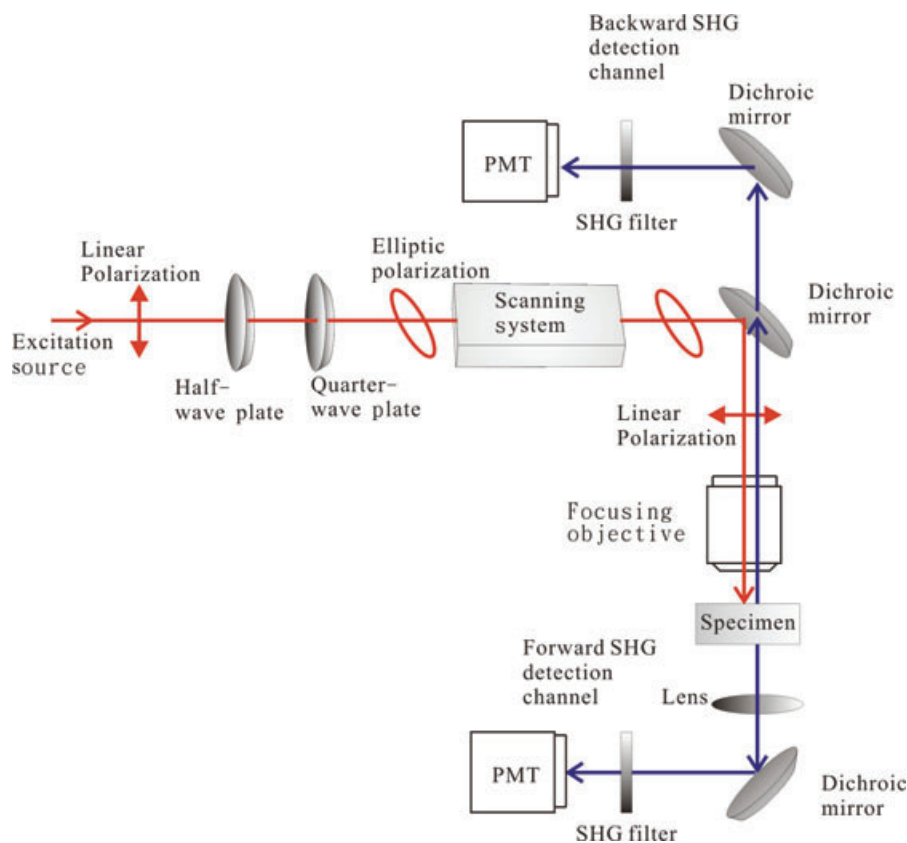


Figure 2 (online color at: www.lpr-journal.org) A typical SHG microscope with both forward and backward detection channels.

eral modifications are made to optimize the optical path, detection geometry, and detection electronics for full exploitation of the SHG contrast mechanism (directionality, polarization) in tissue imaging. Lasers for SHG imaging most commonly consist of a solid state Nd:YAG laser pumped tunable (700 and 1000 nm) titanium sapphire (Ti:Sap) oscillator, where these excitation wavelengths results in imaging abilities of a few hundred microns of tissue thickness.

As described in Sect. 2.2, SHG in tissues is a quasicoherent process where the measured emission directionality depends on the initial spatial distribution and subsequent propagation based on the bulk optical parameters. Therefore, a thorough investigation of the SHG mechanism requires construction of both the epi-illumination path and an efficient, transmitted detection path. As shown in Fig. 2, for detection of the forward signal, the combination of a long working distance water immersion lens (excitation) and a high NA condenser (signal collection) can be used. Both a half wave ($\lambda/2$) and quarter wave plate ($\lambda/4$) are necessary to precisely control the polarization of the laser at the focal plane of the microscope. This level of control is important to perform accurate polarization methods that allow the determination of specimen structural properties. Furthermore, Glan-Laser polarizers, placed in the forward or backward collection paths, are for analysis of the SHG signal polarization that can be used to provide a measure of protein assembly organization [21]. In this collection geometry, the specimen fluorescence signal, if needed, can also be collected in the epi-illuminated path by the use of additional dichroic mirrors and band pass filters. This important con-

sideration in SHG microscopy allows a multimodal imaging scheme to be achieved.

4. SHG-based tissue diagnostics

Since the predominant harmonophores in tissue are types I/II collagen and myosin within actomyosin complexes [25], we will focus our review of SHG imaging of diseased tissues when these protein and assemblies are affected. Collagen I is a major component of connective tissues such as bone, dermis, tendon. Furthermore, muscle cells are wrapped by collagen. It is also the predominant component in the stroma of the breast, ovary, and prostate, and lining of liver capsule, the kidney, and lungs. Therefore, imaging modalities that are sensitive to the assembly of collagen are applicable for diagnosing a broad range of diseases, including connective tissue disorders, musculo-skeletal disorders, and different forms of epithelial cancers. The applications of SHG of pathological tissues are discussed below.

4.1. Connective tissue orders

There are many connective disorders that are characterized by abnormal assembly of fibrillar collagen leading to a broad range of pathologic conditions. These include Osteogenesis imperfecta (brittle bone disease), Marfan's syndrome, Ehler-Danlos syndrome as well as autoimmune conditions including scleroderma, rheumatoid arthritis, and Sjorgren's

syndrome. These and other pathological conditions such as skin photoaging, corneal infection, keratoconus, corneal scar, and atherosclerosis share a common feature in that the assembly of type I collagen (and other supporting collagen) is adversely affected. In some cases, the clinical presentation can be widespread throughout the body. Currently, SHG has been applied to the imaging and characterization of the aforementioned connective tissue disorders and these efforts are reviewed below.

Osteogenesis imperfecta (OI)

OI is a heritable disease of humans characterized by recurrent bone fractures, stunted growth, defective teeth, and other symptoms resulting from abnormal type I collagen tissues [38, 39]. These include visual problems due to an overly thin cornea, heart valve defects, and breathing difficulties from the accompanying and often severe scoliosis. OI results from mutations within the Col1A1 or Col1A2 genes that affect the primary structure of the collagen chain and induce changes in the secondary structure with the ultimate outcome in collagen fibrils that are either abnormally organized, abnormally small, or both.

Campagnola and co-workers have exploited the sensitivity of SHG to supramolecular assembly and to investigate whether this approach can be utilized to differentiate normal and OI tissues using the oim murine model [27, 31]. By comparing SHG intensity, fibrillar morphology, and polarization anisotropy, they found that statistically different results are obtained for the wild type and disease states in bone, tendon, and skin. Representative SHG optical sections of oim and WT bone and skin are shown in Fig. 3. Comparison of the bone cryosections (Fig. 3a) show the diseased tissue is less fibrillar and ordered in appearance, and as a consequence yielded weaker SHG intensity (~ 3 fold). Similarly, the oim skin (Fig. 3b) appears less ordered and was characterized by larger Δk values [26]. All the optical signatures from SHG imaging are consistent with the collagen matrix in the oim tissues being increasingly disordered and mechanically weaker in vivo. To further quantify differences in the tissue structure, they utilized a set of parameters comprised of the SHG creation attributes (emission directionality and conversion efficiency) and the bulk optical parameters (scattering coefficient μ_s and scattering anisotropy, g), all of which are related to the collagen fibrillar assembly [27]. This approach allows for estimation of the SHG creation attributes and separation of primary (loss of laser) and secondary filter (loss of SHG signal based on bulk optical parameters) effects. Structural dissimilarities between the oim and WT tissues led to statistically significant differences in the SHG conversion efficiency (2.9 fold larger for the WT; $p < 0.005$), which is related to collagen organization. Similarly, the SHG depth-dependent directionality and forward signal attenuation are statistically different for the WT and oim dermis. The use of Monte Carlo simulations allows the decoupling of the SHG creation attributes and subsequent propagation (based on μ_s and g), where these photons are experimentally indistinguishable.

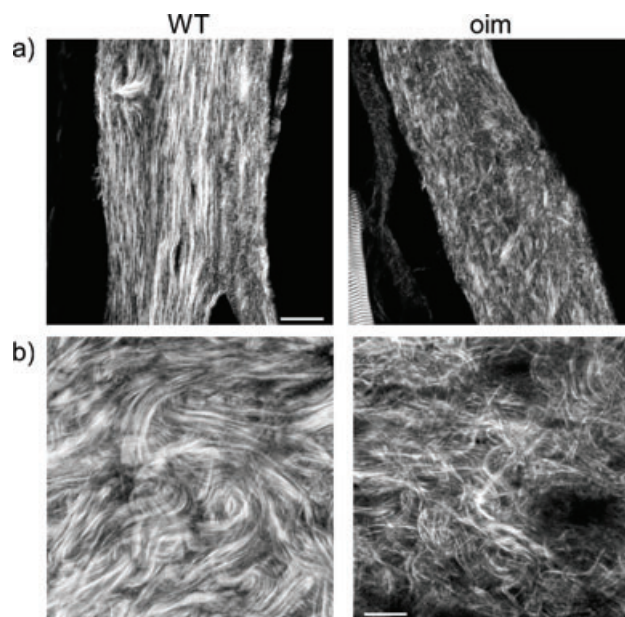


Figure 3 Representative SHG single optical sections from WT (left panels) and oim (right) murine tissues, where a) are 6 micron thick cryosections of de-mineralized femur and b) are from skin biopsies. The diseased tissues are more disordered. Scale bar = 20 microns.

They suggested that these results were consistent with the observed phenotype in each genotype, and it seems that this optical scheme could be used in lieu of existing invasive and destructive methods. These methods may be especially useful in monitoring the status of individual patients relative to their initial screen, where patients would already have a genetic profile. In addition, this approach may permit monitoring the efficacy of treatment. For example, the effect of treatment with bis-phosphonates has been typically performed by bulk bone density and mineralization measurements [40].

Dermal photoaging

While UV exposure is believed to be a main contributor of skin photoaging, in the clinic, a real-time diagnostic tool for the direct, label-free diagnosis of the degree of photoaging is lacking. Morphologically, a number of symptoms such as pigmentation irregularity, dryness, and wrinkle formation are associated with skin aging. Microscopically, as a person ages, the content of connective tissues within the dermis also changes, where the density of collagen fibers decreases and become replaced by elastic fibers [41]. The fact that the skin dermis is composed primarily of collagen and elastic fibers points at the possibility of using nonlinear optical signals for assessing the extent of skin photoaging. Specifically, collagen fibers are strong generators of the second harmonic signal, whereas elastic fibers are only autofluorescent. Therefore, the use of a single excitation wavelength could produce the SHG signal and multiphoton autofluorescence (MAF) signals for the respective detection of these

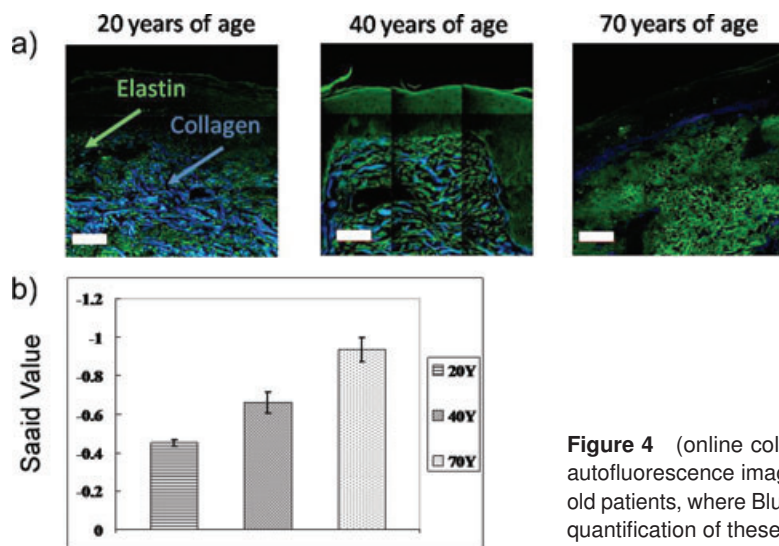


Figure 4 (online color at: www.lpr-journal.org) a) SHG and multiphoton autofluorescence imaging of *ex-vivo* human dermis in 20, 40, and 70 years-old patients, where Blue = SHG and green = autofluorescence. b) Skin aging quantification of these tissues using the SAAID metric (from [42]).

components. In this regard, Lin et al. realized this potential for evaluating different extents of skin photoaging by spectrally separating these two signals, demonstrated this concept in *ex-vivo* skin specimens from individuals of 20, 40, and 70 years of age [42]. As shown in Fig. 4a, the SHG collagen fibers are in greater abundance in the 20 years-old whereas autofluorescent elastic fibers are the prominent feature in the dermis of the 70 years-old. In addition to qualitative examination, a numerical index was derived in an attempt to quantify the observed photoaging effect. The SHG-autofluorescence aging index (SAAID) is defined as:

$$\text{SAAID} = \frac{\text{SHG} - \text{MAF}}{\text{SHG} + \text{MAF}} \quad (8)$$

where SHG and MAF represents the pixel numbers of the respective SHG and MAF signals that are above preselected threshold intensities. The use of the pixel-counting approach rather than using absolute SHG and MAF intensities is advantageous in deep-tissue imaging applications where the absolute SHG and MAF signal intensities can be erroneously affected by tissue scattering and specimen induced spherical aberration. On the contrary, the use of appropriately selected background intensity would render the pixel-counting approach virtually artifact-free. According to this definition, an elder person would have a more negative SAAID value since the dermis of such an individual is expected to have a higher elastic fiber than collagen fiber content. Analysis of the SHG and MAF images of the dermis from the 20, 40, and 70 years-old individuals is shown in Fig. 4b where as a person ages, the SAAID progressively decreased and reached a value of -0.93 for the 70 years-old patient [42]. Thus this analysis shows the expected tendency. Therefore, the unique combination of SHG and broadband MAF imaging demonstrates that label-free, multiphoton imaging can be used for the effective quantitative characterization of skin photoaging. Later, this diagnostic approach was extended to *in vivo* studies in 18 patients and the results show the same correlation between the SAAID parameter with aging as the *ex-vivo* study. Furthermore, these inves-

tigators found a stronger dependence of the SAAID index among female patients [43].

Pathological conditions of the cornea

Another connective tissue to which SHG imaging can be powerfully applied is the cornea stroma. As the front-most component of the human vision system, the cornea, with nominal thickness of around $520\mu\text{m}$, is responsible for most of the refractive properties of the eye. The unique optical properties of the cornea (90% visible light transmission) [44, 45] hinder standard one-photon microscopic imaging modalities to be applied effectively. While reflected confocal microscopy has been demonstrated to be an effective technique for imaging the corneal epithelium [46], the collagenous stroma, the main component of the cornea, is virtually invisible to one-photon techniques. Furthermore, due to the importance of cornea in vision, the application of traditional histological procedures for diagnosing corneal pathologies is not feasible. These circumstances create a dilemma in ophthalmic pathological diagnosis, where physicians often need to perform time-consuming, *in vitro* culturing studies in order to determine the responsible pathogens before prescribing effective treatment procedures. This identification can take up to around a week, resulting in the loss of valuable diagnostic time. Thus there is a clear need in to develop a non-invasive imaging modality that can be used for corneal pathological diagnosis. Since the composition of corneal stroma is mostly type I collagen [44], SHG microscopy is a natural choice for the label-free imaging and diagnosis of pathological degradations of the corneal architecture.

The usefulness of SHG imaging in corneal imaging was first recognized by Tromberg's group. By the use of MAF and SHG microscopy in the backscattering geometry, they recognized that it was possible to image stromal collagen and differentiate this matrix from the epithelial cells and keratocytes in rabbit corneas [5]. Later, Teng et al. performed

additional experiments and demonstrated that the combination of MAF and backward SHG imaging can be used to image various structures of the ocular surface in intact, *ex-vivo* porcine eyes [47]. Specifically, it was shown that the MAF signal can be used to delineate the corneal epithelium, the underlying inner layer, the limbus, and the conjunctiva. On the other hand, SHG imaging was effective in imaging the collagen matrix of the corneal stroma and sclera. Their study also demonstrated that while backward SHG imaging is capable of imaging throughout the entire corneal thickness, the inherent opacity significantly limits sclera imaging to a depth of around 200 μm .

The large-area imaging approach utilized in that work was later applied by Lo et al. to achieve multiphoton fluorescence and SHG imaging across the entire cornea of a GFP mouse, providing the global organization of tissue under investigation with high-resolution. These authors demonstrated that mouse cornea is organized into overlapping layers parallel to the corneal surface [48].

However, an important issue that remains to be resolved is the morphological differences observed between forward and backward SHG images of the cornea. Han et al. showed that while the forward and backward SHG images of the less organized, optically opaque sclera reveal similar collagen fiber structures, forward and backward SHG imaging show considerable dissimilarities [12]. Specifically forward SHG imaging show the fibrous organization of the cornea, whereas the contrast seen in backward SHG imaging consists of diffuse structures. Since backward SHG imaging is the clinically relevant imaging modality, this issue needs to be resolved in order for SHG microscopy to become a clinically viable technique for corneal disease diagnosis.

At the present, different groups have successfully applied SHG and multiphoton fluorescence microscopy to characterize the extent of corneal disease progression *ex vivo*. Infectious keratitis is one example in which the combination of SHG and MAF imaging has been successfully applied. In the work by Tan et al., it was shown that SHG imaging can be used to characterize collagen disruption while the MAF signal can be simultaneously used for the label-free, morphological identification of infectious pathogens [49]. This approach has been applied for the characterization of cases of bacterial (*Serratia marcescens*), fungal (*Alternaria*), and protozoa/bacterial (*Acanthamoeba/Pseudomonas aeruginosa*) infected corneas under *ex-vivo* conditions.

Another interesting pathological condition that has been investigated by SHG imaging is keratoconus, i.e. the abnormal reorganization of corneal collagen possibly due to insufficient cross-linking between neighboring collagen fibers. By using SHG and MAF, Tan et al. showed that the global reorganization of corneal collagen can be characterized by the SHG signal [50]. They found that the morphological features obtained from whole-cornea multiphoton imaging were consistent with topographic mapping associated with standard clinical diagnosis. Furthermore, they found that near the keratoconical apex, corneal cells tend to align parallel to the direction of altered collagen lamellae and become spindle-like in shape, indicating that collagen reorganization can substantially affect local cell morphology [50]. A later

study using SHG imaging revealed that abnormal collagen organization occurred in the anterior stroma [51].

Additional corneal pathologies are related to irregularity in corneal collagen organization in scars arising from damage or refractive surgery procedure for vision correction. In the first case, Teng et al., showed that the compromised structure of Bowman's layer and in-depth collagen orientation parallel to the wound edge can be imaged without external labeling [52]. In another interesting study, Brown et al. showed that SHG imaging can be used to monitor collagen movement in the optical nerve head due to intraocular pressure [53]. In the second case, the effect of scarring following photorefractive keratectomy (PRK) is an area of concern. This procedure is one of the major techniques used to treat myopia patients, where a laser is used to remove extra corneal stroma, forming a more negative lens thus allowing focusing onto the retina. However, effects such as haze formation can be an issue. To investigate whether SHG microscopy can be used to characterize corneas undergoing the PRK procedures, Farid et al. successfully imaged the fibrosis process following excimer laser ablation [54]. In addition, they showed that mitomycin C treatment significantly reduces the formation of corneal haze.

Atherosclerosis

Cardiovascular diseases including heart attack and stroke remain the most common form of death in the US. Atherosclerosis, or the buildup of arterial plaques consisting of extracellular deposits of low density lipids (LDLs) are an integral part of the process, which gradually develops over a period of many years. Current clinical methods such as ultrasound and MRI do not have sufficient resolution to follow the structural changes in the elastin/collagen composition of the arterial lumen. While OCT can measure changes in plaque density it lacks the specificity needed to follow biochemical changes in the composition. It has recently been suggested that SHG in multimodal approaches may be suitable for imaging both changes in arterial wall structure and composition.

Using tissues from Ossabaw swine which represent metabolic syndrome induced plaques, Cheng and co-workers used SHG in conjunction with MAF and CARS to compare the elastin/collagen distribution in normal tissues against those in lesion [55]. They found that the elastin barrier which is believed to prevent penetration of LDL droplets, was continuous in the normal case but intermingled with collagen in the lesions. Additionally, dense fibrillar collagen was located across the elastic barrier near the lumen surface, where the organization was different than the distal side. Using CARS and MAF, they also identified LDL droplets and lipid rich cells on the proximal side of the lumen. The authors suggest that understanding changes in structure and composition at this level of resolution and specificity may identify areas at risk of rupture and lead to specific treatments based on these alterations. These ideas were also examined in mouse and pig models by Balaban [18]. It had been suggested that branch points may be most susceptible

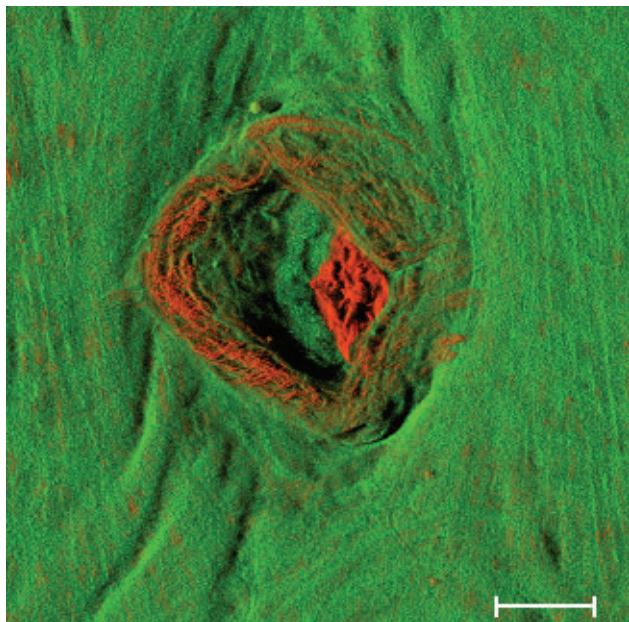


Figure 5 (online color at: www.lpr-journal.org) 3D rendering of atherosclerosis-susceptible intervertebral branch point with a ring of exposed collagen around the ostia. Red = elastin auto-fluorescence and Green = collagen SHG. Scale bar = 50 microns. (courtesy Dr. Robert Balaban.)

to plaque formation, where it was hypothesized that local wall stress and turbulence heterogeneities were responsible. Using SHG and MAF imaging of collagen and elastin, respectively, they showed there was no clear elastin barrier at the branchpoints, where the elastin was mingled with dense collagen (Fig. 5). They also found that LDL preferentially binds at the branches due to increased collagen levels. This study showed that mechanical considerations alone are not sufficient to understand risk of rupture, and that local changes in biochemical composition must also be considered.

Sjogrens syndrome

Sjogren's syndrome (SS) is an autoimmune disease characterized by dry mouth, dry eye, and arthritis. While the underlying mechanisms that trigger the onset of the disease are not known, it is understood that the extracellular matrix (ECM) in the salivary and lacrimal glands is degraded. Schenke-Layland used SHG to examine changes in the lacrimal gland using a NOD (non-obese diabetic) mouse model, which displays many of the phenotypic features of SS [56]. They observed a significant decrease (~ 3.5 fold) in the SHG intensity in the NOD relative to the WT. Moreover, SHG revealed a larger change in the collagen assembly than displayed by histology, suggesting increased sensitivity over the latter method, concurrent with the ability to image un-labeled tissues. The authors suggested that SHG imaging may provide new insight into the progressive degeneration of the ECM in Sjogren's syndrome and that this may lead to new therapeutic approaches [56].

Collagen thermal denaturation in connective tissues

An important application of SHG imaging is collagen thermal denaturation in connective tissues, as, for example, this is related to damage in burn victims. Although collagen degradation has been previously studied by SHG where a denaturation temperature of 64°C was measured [57], the mechanism of damage cannot be completely understood without detailed microscopic imaging. As a first step using rat tail tendon, researchers used qualitative imaging and quantitative SHG analysis to characterize this process. By heating the collagen specimens between 25 – 60°C , it was found that SHG intensity begins to decrease at 45°C . In addition, it was found that collagen fibers did not degrade uniformly, where the SHG signal starts to vanish within localized regions starting at 57°C , leading to banded patterns of SHG signals and at 60°C , the SHG intensity degraded to an insignificantly level [58]. Later, a more thorough study found that imaging at different spatial scales reveals that rat tail tendon undergoes thermal denaturation by two processes [59]. First, there are localized structurally weak points that are more easily susceptible to thermal damage and that the thermal damage will expand from these weak points. Secondly, there is a global denaturation process that occurs throughout the collagen fiber matrix [58].

In addition to the ability of SHG imaging for studying the underlying biophysics of collagen thermal denaturation, there are also medical consequences of such work. While thermal treatment is now commonplace for treating conditions such as aging skin, a quantitative metric characterizing the extent of skin contraction is lacking. To address this issue in a model system researchers heated rat tail tendon to detect the dependence of tendon length as a function of SHG intensity and found there is a shrinkage associated with a decrease in SHG intensity [60]. They found a linear relationship between the change in relative length to the relative change in SHG intensity. Therefore, SHG imaging not only can be used to characterize the extent of collagen thermal damage, the relative change in intensity can also be used to quantify the extent of tissue shrinkage.

This analysis can be applied to examine thermal damage of the collagen and elastin in dermis. For example, using human foreskin dermis, Lin et al. found that for temperatures at and above 60°C , the SHG intensity from the collagen fibers decreased [61]. However, there was a corresponding increase in the MAF intensity. Furthermore, the elastic fibers begin to break and aggregate starting at 65°C . While variation in the distribution of collagen and elastic fibers in the samples can affect detected MAF or SHG signals, the ratio of MAF/SHG (SAAID index) showed a consistent increase above 60°C . This observation supports the fact that the threshold of skin dermis starts at 60°C .

Thermal effects on collagen rich tissues are also important issues for the cornea as conditions such as myopia and presbyopia can now be treated with photophysical processes such as laser and thermal treatment. However, one always needs to be concerned with the thermal effects of these processes. As a first step Tan and coworkers investigated

the feasibility of characterizing the thermal denaturation of corneal stroma by SHG imaging and quantification [62]. By heating porcine corneas they found that at sufficiently high temperatures (90 °C), the backward SHG intensity significantly decreased, representing complete collagen denaturation. Now SHG has been used to examine the cornea following conductive keratoplasty (CK). In this technique, pins are inserted at corneal periphery of presbyopia patients and through RF application the corneas under treatment would swell and make a more positive lens which results in vision correction. However, as a new technique, a number of issues such as regression remain to be characterized. In this effort, Wang et al. monitored the wounding healing process in rabbit corneas at Day 1, Weeks 1, 2, and 4 after the CK procedure. In control case corneas (no RF), the wound quickly healed and at Week 1, the surgery site could barely be identified by SHG/MAF imaging. By contrast, in CK corneas, epithelial hyperplasia into the stroma and irregular regeneration of the stroma collagen at the wounding site was clearly evident, where the corneal collagen was organized in a radial pattern contracting towards the wounding site. Recently Pavone and coworkers showed a new method to quantify the similar resulting disorder in the collagen structure in the cornea following laser welding [63]. Collectively these results demonstrate the feasibility of using SHG/MAF imaging in probing the effects of refractive surgical procedures and provide insights into the subsequent wound healing process [64].

Diagnosis of abnormalities of collagen assembly in other tissues

Since excessive collagen generation often marks pathological conditions associated with specific organs, SHG imaging seems to be the ideal technique for evaluating the extent of organ fibrosis. For example, Strupler et al. demonstrated the applicability of SHG analysis in renal fibrosis [65]. In addition, since normal lung tissues are rich in collagen and elastic fibers, the combination of SHG and MAF imaging has been demonstrated by Wang et al. to be effective for distinguishing between non-cancerous and autofluorescent lung tumor masses such as lung adenocarcinoma [66]. Additionally liver fibrosis can be easily diagnosed, where the morphological feature associated with the METAVIR grading system can be easily achieved without extrinsic labeling [67, 68].

4.2. Musculo-skeletal disorders

Due to its sensitivity to structure, SHG can also be used to examine musculoskeletal pathologies, where these could be in the form of congenital diseases such as muscular dystrophies or skeletal injuries. In addition to simply visualizing the structures of either collagen fibrils or myofibrils, quantitative metrics are necessary to assess disease severity/progression or extent of injury. Here, we review recently presented approaches to this class of problem.

Spinal damage

Reiser and co-workers have applied two distinct analytic approaches to quantify inter-vertebral disk damage in a mouse model. In both of these efforts, a needle was inserted into one of the vertebrae and then the spine was loaded to strain the disk. Their first analysis created a “disorder map” to compare small regions of damage and to isolate boundaries of the injury [69]. This was achieved by creating a matrix of a small number of fibrils (e.g. 3×3) and quantifying the extent of fibril alignment, where deviations from normal alignment are indicative of damage. This approach was able to discern the damaged disks of loaded versus sham loaded mice. The second approach employed by these investigators used spectral moment analysis [70]. As this is derived directly from the 2D Fourier spectrum, this approach is insensitive to scale or scan geometries, unlike other approaches such as wavelet transform analysis (or their previous approach). The authors found that the linear discriminate classifier provided significantly different results for normal and loaded disk. Moreover, they suggested this approach may be more generally applicable to complex tissues without significant fibril alignment.

Muscle disorders

Mohler and Campagnola have applied quantitative image analysis techniques of SHG data to score the severity of disease in several mouse models of muscle disorders [71]. In healthy fibers, bands of sarcomeres are straight and evenly spaced ($\sim 2\text{--}3$ microns), with each band lying virtually orthogonal to the axis of contraction. Damaged cells display a range of visible deviations from this norm, and an individual region of sarcomere bands can be found to display any one or a combination of these defects. To measure changes in disease models, they applied the Helmholtz equation for wave number to calculate the local striation spacing and angle of orientation with respect to the long axis of the myofiber (90° for ideal case). In addition to the primary SHG intensity map, this step creates new image maps for these two metrics. They tested this sarcomere pattern quantification (SPQ) approach by comparing controls to three models of muscular disorders: disuse-induced atrophy, hereditary muscular dystrophy (mild (mdx) and severe (mdx/UTR) forms) and sarcopenia of aging. These models each incur a characteristic degree of damage within the full spectrum of phenotypic severity, allowing the rating of the sensitivity of SHG image analysis in detecting injury. A consistently negative correlation was revealed between severity of the disorder and the mean sarcomere length for all disorder models tested. Both mild and severe forms of MDs caused substantial reduction of the range of sarcomere lengths and yielded an increased fraction of hyper-contracted sarcomeres. To verify usefulness of the diagnostic procedure and accuracy of the SPQ scores, they performed receiver operating characteristic (ROC) analysis, using both non-parametric and multivariate logistic regression, to assess the efficacy of a given variable in distinguishing the normal and diseased tissue. They found

that several disease-to-control SPQ comparisons, with sample sizes of 5 to 10 mice per condition, gave ROC area under the curve with a 95%-lower-confidence-bound above 0.74, indicating a strong diagnostic test. The authors argued that existing imaging modalities using EM, histological staining, or polarization microscopy cannot provide this quantity of data, as single sections need to be sliced and prepared, whereas SHG can image through tissue biopsies of several hundred microns of thickness.

4.3. Diagnosis of epithelial cancers

A broad area of potential SHG clinical application lies in the early detection of cancers. It now is well appreciated that interactions between tumor and stromal compartments play an important role in tumor progression, where in addition to changes in the epithelial cells, the stromal extracellular matrix is altered during the progression of many epithelial cancers. Increased synthesis of type I collagen surrounding tumors, termed desmoplasia, is associated with poor prognosis in breast, prostate and colon cancer.

Skin cancer imaging

Basal cell carcinoma (BCC), a common type of skin malignancy, forms nodular aggregates within the dermis. Clinically, physicians rely on techniques such as Moh's surgery for the sequential removal and diagnosis of the affected tissues. Clearly, a direct diagnostic approach that allows real-time monitoring of the tumor edge would be time and tissue saving. The possibility of using SHG and MAF imaging in this effort has been demonstrated on *ex-vivo* BCC specimens by different groups [11, 72, 73]. As shown in Fig. 6a, the nodular BCC tumor masses composed of densely packed cancer cells can be clearly delineated from the surrounding, non-cancerous dermis, where blue and green are SHG and autofluorescence, respectively. Comparison with H&E histological images taken from adjacent tissue sections (Fig. 6b) demonstrates that the combination of SHG and MAF microscopy is capable of detecting the tumor masses without extrinsic labeling. In addition to qualitative imaging, the indexing approach described in Eqn. (9) can also be used to analyze alterations of dermal content from tumor invasion. From the multiphoton images, one sees that the distribution

of collagen fibers primarily lies in the normal stroma far away from the tumor masses and that MAF signal dominates at the tumor sites and dermis near the tumor. For the purpose of quantification, regions from within the tumor, at the tumor dermis, and at the normal dermis were selected. An inverse definition of the SAAID definition shows that as one moves away from the tumor regions, the SHG-MAF index decreases indicating the presence of higher collagen content. Specifically, within the tumor region, the index is 0.93 indicating that the tumor is composed primarily of cancer cells. This observation demonstrates the fact that a higher content of collagen fibers is found in regions distant from the tumor masses, corroborating the postulation that up-regulated metalloprotease (MMP) activity of invading tumors can alter the ECM of surrounding normal tissues.

Breast cancer

To investigate if SHG is a useful early diagnostic of breast cancer, using mouse models, Keely et al. defined changes in collagen structure associated with tumors visualized *in situ*. They specifically noted increased collagen deposition (desmoplasia) near early pre-palpable tumors, as well as realignment of the collagen fibers with respect to the tumor boundary. In these efforts they characterized three "Tumor-Associated Collagen Signatures (TACS)," which are reproducible defined stages of tumor progression [74, 75], where these signatures are characterized by (i) the presence of dense collagen localized around small tumors during early disease, (ii) collagen fibers that are parallel to the tumor boundary; and (iii) collagen fibers that are normal to the tumor boundary for invasive disease. Representative images for these "TACS" are shown in the Fig. 7 (courtesy Keely).

The increase in local collagen deposition is particularly relevant to investigations of invasion and metastasis, as tumor cells migrate through and along collagen matrices. For example, in an elegant study, Condeelis and coworkers visualized *in vivo* the differential migration of cells of differing metastatic potential, where the metastatic cells migrated specifically along fibers [76]. These results demonstrate the usefulness of developing SHG approaches in the context of understanding breast cancer biology, where these insights may be applicable to human cancers as well. Moreover, 85% of all cancers are epithelial in nature, and there is increasing evidence that remodeling of the underlying ECM may be

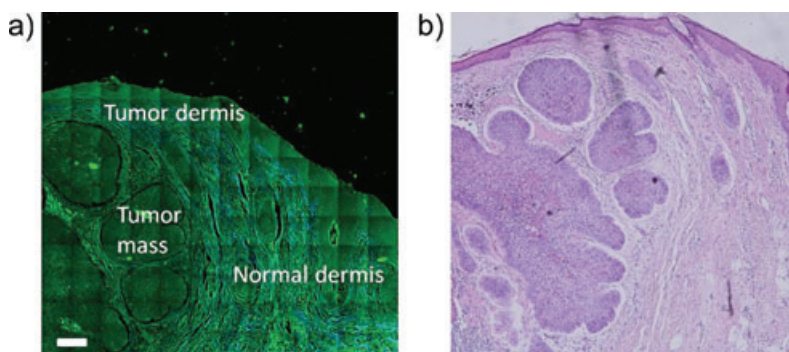


Figure 6 (online color at: www.lpr-journal.org) Optical diagnosis of *ex-vivo* human basal cell carcinoma using a) SHG and multiphoton autofluorescence imaging, where blue = SHG, green = autofluorescence and b) adjacent H&E histological section (from [11]).

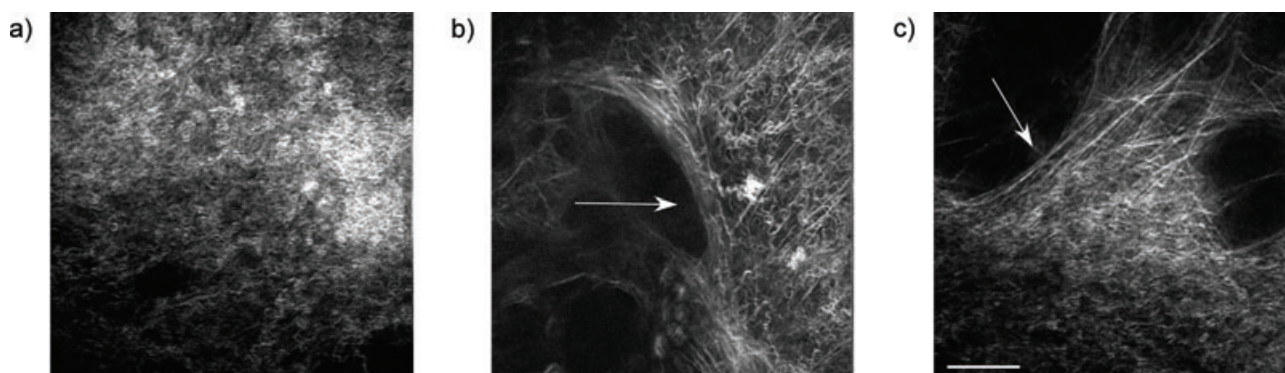


Figure 7 Representative images of tumor associated collagen signatures (TACS) in a mouse breast cancer model, where a,b,c, and correspond to TACS 1, 2, and 3, respectively. The arrows in (b) and (c) delineate the tumor boundary (courtesy Prof. Patricia Keely). Scale bar = 50 microns.

a common aspect of carcinogenesis. For example, cervical pre-cancer has early changes in structural protein assembly prior to cancer [77], ii) in prostate there is alteration in the stromal microenvironment which is sufficient to promote malignant transformation of the epithelial cells [78]; iii) colon studies have shown that the ECM and the conditioned medium from colon carcinoma support and catalyze the conversion of normal epithelial to carcinoma cells [79]; and iv) Jain observed increased collagen in a mouse model of human melanoma [80].

5. Perspectives and outlook

In this article we have attempted to sample the breadth of how SHG imaging may be applied as an imaging diagnostic tool. As demonstrated, numerous pathologies including connective tissue disorders, musculoskeletal disorders, cancers, and organ fibrosis can be examined. Not only can pathological diagnosis be performed, issues related to fundamental biological processes can also be investigated using SHG imaging.

Before full translation to clinical applications can occur, there are several areas that are in need of improvement for practical implementations. First, the SHG imaging instrumentation needs to be made compatible with clinical practices in terms of size and user-friendliness. “Turn-key” Ti:Sap lasers are now commercially available and small footprint solid state platforms at specific wavelengths are also on the market. Advances in photonic crystal fibers and GRIN lens technology have been combined with miniaturized scanning systems, allowing femtosecond-pulsed multiphoton fluorescence imaging through microendoscopes with diameters of less than one millimeter which will afford true *in vivo* image acquisition. For example, Llewellyn et al. recently demonstrated that minimally invasive microendoscopy could be used to measure changes in sarcomere lengths by SHG imaging in a live mouse [81, 82].

An additional area of improvement will come in the form of obtaining increased imaging depth. With the available excitation wavelengths from Ti:sapphire oscillators of around 700–1000 nm, imaging depths in highly scattering

tissues are limited to a few hundred microns at best. The Campagnola lab has shown that the loss of the laser due to scattering, i.e. the primary filter effect, is the dominant factor in these limits [27, 30]. These depth limitations due to scattering can be extended through the use of adaptive optics or optical clearing. In the former case, a multi-element micro-mirror is used to compensate for specimen induced aberrations that become increasingly important with increasing imaging depth into tissue. Optical clearing utilizes the application of a hyper-osmotic agent to tissues, which through refractive index matching, reduces the scattering coefficient and increases the mean free path [83]. Optical clearing has been shown to increase the capabilities of two-photon [84] and SHG collagen imaging [30, 85]. Adaptive optics has now been demonstrated for CARS [86] and two-photon imaging [87]. Additionally, longer wavelength lasers will become more widely commercially available.

In addition to these instrument-based areas, SHG applications will be enhanced by the continued development and refinement of methods to obtain objective, quantitative information. These will be in the form of analysis algorithms such as Helmholtz analysis, wavelet analysis, and texture analysis. A further understanding of the SHG physics and its relationship to tissue assembly will also allow the extraction of more detailed and quantitative information from image data.

With the exciting and recent technical development of SHG imaging and the continuing exploration of pathological tissues that can be examined by this technique, it is conceivable that in the near future, SHG could become a useful diagnostic technique in the clinic capable of providing real time surgical decisions, selecting the tissue area to biopsy, and still allow fundamental biological questions to be addressed.

Acknowledgements. PJC gratefully acknowledges support under NIH EB1842. C.Y. Dong acknowledges the support of the National Research Program for Genomic Project of the National Science Council in Taiwan. We thank Prof. Patti Keely, Dr. Robert Balaban, and Dr. Ping-Jung Su for providing images.

Received: 30 April 2009, **Revised:** 20 July 2009, **Accepted:** 30 July 2009

Published online: 15 October 2009

Key words: Second harmonic generation, collagen, muscle, diseases.



Paul J. Campagnola received his PhD in physical chemistry from Yale in 1992 and was a postdoctoral fellow at the University of Colorado. In 1992 he then joined the faculty at the University of Connecticut Health Center. He has been developing Second Harmonic Generation imaging microscopy with an emphasis on implementing quantitative metrics for diagnosing cancer and connective tissue disorders. A second research area uses nano/microfabrication for tissue engineering and cancer biology applications.



Chen-Yuan Dong received his PhD in physics from the University of Illinois at Urbana-Champaign in 1998 under Enrico Gratton. Between 1998 and 2000, he was an NIH postdoctoral fellow at MIT where he worked with Peter So in applying multiphoton microscopy for tissue imaging. He joined the Department of Physics at National Taiwan University in 2001 where he has been developing multiphoton imaging for biomedical research with the specific focus on understanding intravital physiological phenomena and biophysics.

References

- [1] I. Freund, M. Deutsch, and A. Sprecher, *Biophys. J.* **50**, 693–712 (1986).
- [2] C. J. R. Sheppard, R. Kompfner, J. Gannaway, and D. Walsh, *IEEE J. Quantum Electron.* **13E**, 100D (1977).
- [3] S.-P. Tai, T.-H. Tsai, W.-J. Lee, D.-B. Shieh, Y.-H. Liao, H.-Y. Huang, K. Zhang, H.-L. Liu, and C.-K. Sun, *Opt. Express* **13**, 8231–8242 (2005).
- [4] A. Zoumi, X. Lu, G. S. Kassab, and B. J. Tromberg, *Biophys. J.* **87**, 2778–2786 (2004).
- [5] A. T. Yeh, N. Nassif, A. Zoumi, and B. J. Tromberg, *Opt. Lett.* **27**, 2082–2084 (2002).
- [6] R. M. Williams, W. R. Zipfel, and W. W. Webb, *Biophys. J.* **88**, 1377–1386 (2005).
- [7] T. A. Theodossiou, C. Thrasivoulou, C. Ekwobi, and D. L. Becker, *Biophys. J.* **91**, 4665–4677 (2006).
- [8] A. T. Yeh, B. Choi, J. S. Nelson, and B. J. Tromberg, *J. Invest. Dermatol.* **121**, 1332–1335 (2003).
- [9] P. Stoller, B.-M. Kim, A. M. Rubinchik, K. M. Reiser, and L. B. Da Silva, *J. Biomed. Opt.* **7**, 205–214 (2001).
- [10] P. Stoller, K. M. Reiser, P. M. Celliers, and A. M. Rubinchik, *Biophys. J.* **82**, 3330–3342 (2002).
- [11] S. J. Lin, S. H. Jee, C. J. Kuo, R. J. Wu, W. C. Lin, J. S. Chen, Y. H. Liao, C. J. Hsu, T. F. Tsai, Y. F. Chen, and C. Y. Dong, *Opt. Lett.* **31**, 2756–2758 (2006).
- [12] M. Han, G. Giese, and J. F. Bille, *Opt. Express* **13**, 5791–5797 (2005).
- [13] M. Han, L. Zickler, G. Giese, M. Walter, F. H. Loesel, and J. F. Bille, *J. Biomed. Opt.* **9**, 760–766 (2004).
- [14] G. Cox, E. Kable, A. Jones, I. Fraser, F. Manconi, and M. D. Gorrell, *J. Struct. Biol.* **141**, 53–62 (2003).
- [15] A. M. Pena, A. Fabre, D. Debarre, J. Marchal-Somme, B. Crestani, J. L. Martin, E. Beaurepaire, and M. C. Schanne-Klein, *Microsc. Res. Tech.* **70**, 162–170 (2007).
- [16] J. L. Drury and D. J. Mooney, *Biomaterials* **24**, 4337–4351 (2003).
- [17] C. Odin, Y. Le Grand, A. Renault, L. Gailhouste, and G. Baf-fet, *J. Microsc.* **229**, 32–38 (2008).
- [18] G. P. Kwon, J. L. Schroeder, M. J. Amar, A. T. Remaley, and R. S. Balaban, *Circulation* **117**, 2919–2927 (2008).
- [19] S. Ramanujan, A. Pluen, T. D. McKee, E. B. Brown, Y. Boucher, and R. K. Jain, *Biophys. J.* **83**, 1650–1660 (2002).
- [20] A. Zoumi, A. Yeh, and B. J. Tromberg, *Proc. Natl. Acad. Sci. USA* **99**, 11014–11019 (2002).
- [21] P. J. Campagnola, A. C. Millard, M. Terasaki, P. E. Hoppe, C. J. Malone, and W. A. Mohler, *Biophys. J.* **82**, 493–508 (2002).
- [22] S.-W. Chu, S.-Y. Chen, G.-W. Chern, T.-H. Tsai, Y.-C. Chen, B.-L. Lin, and C.-K. Sun, *Biophys. J.* **86**, 3914–3922 (2004).
- [23] D. A. Dombeck, K. A. Kasischke, H. D. Vishwasrao, M. Ingelsson, B. T. Hyman, and W. W. Webb, *Proc. Natl. Acad. Sci. USA* **100**, 7081–7086 (2003).
- [24] F. Vanzi, M. Capitanio, L. Sacconi, C. Stringari, R. Cicchi, M. Canepari, M. Maffei, N. Piroddi, C. Poggesi, V. Nucciotti, M. Linari, G. Piazzesi, C. Tesi, R. Antolini, V. Lombardi, R. Bottinelli, and F. S. Pavone, *J. Muscle. Res. Cell. Motil.* **27**, 469–479 (2006).
- [25] S. V. Plotnikov, A. C. Millard, P. J. Campagnola, and W. A. Mohler, *Biophys. J.* **90**, 693–703 (2006).
- [26] R. Lacomb, O. Nadiarnykh, S. S. Townsend, and P. J. Campagnola, *Opt. Commun.* **281**, 1823–1832 (2008).
- [27] R. Lacomb, O. Nadiarnykh, and P. J. Campagnola, *Biophys. J.* **94**, 4104–4104 (2008).
- [28] J. Mertz and L. Moreaux, *Opt. Commun.* **196**, 325–330 (2001).
- [29] O. Nadiarnykh, R. B. LaComb, P. J. Campagnola, and W. A. Mohler, *Opt. Express* **15**, 3348–3360 (2007).
- [30] R. LaComb, O. Nadiarnykh, S. Carey, and P. J. Campagnola, *J. Biomed. Opt.* **13**, 021108 (2008).
- [31] O. Nadiarnykh, S. Plotnikov, W. A. Mohler, I. Kalajzic, D. Redford-Badwal, and P. J. Campagnola, *J. Biomed. Opt.* **12**, 051805 (2007).
- [32] J. M. Hicks and T. Petralli-Mallow, *Appl. Phys. B* **68**, 589–593 (1999).
- [33] T. Verbiest, M. Kauranen, A. Persoons, M. Ikonen, J. Kurkela, and H. Lemmetyinen, *J. Am. Chem. Soc.* **116**, 9203–9205 (1994).
- [34] T. Verbiest, S. V. Elshocht, M. Kauranen, L. Hellemans, J. Snauwaert, C. Nuckolls, T. J. Katz, and A. Persoons, *Science* **282**, 913–915 (1998).
- [35] Y. Fu, H. Wang, R. Shi, and J. X. Cheng, *Biophys. J.* **92**, 3251–3259 (2007).
- [36] I. Rocha-Mendoza, D. R. Yankelevich, M. Wang, K. M. Reiser, C. W. Frank, and A. Knoesen, *Biophys. J.* **93**, 4433–4444 (2007).
- [37] A. M. Pena, T. Boulesteix, T. Dartigalongue, and M. C. Schanne-Klein, *J. Am. Chem. Soc.* **127**, 10314–10322 (2005).
- [38] J. Baum and B. Brodsky, *Curr. Opin. Struct. Biol.* **9**, 122–128 (1999).

- [39] S. D. Chipman, H. O. Sweet, D. J. McBride, Jr., M. T. Davisson, S. C. Marks, Jr., A. R. Shuldiner, R. J. Wenstrup, D. W. Rowe, and J. R. Shapiro, *Proc. Natl. Acad. Sci. USA* **90**, 1701–1705 (1993).
- [40] E. A. McCarthy, C. L. Raggio, M. D. Hossack, E. A. Miller, S. Jain, A. L. Boskey, and N. P. Camacho, *Pediatr. Res.* **52**, 660–670 (2002).
- [41] M. Yarr and B. Gilchrist, *Fitzpatrick's Dermatology in General Medicine* (McGraw-Hill, Columbus, OH, 2003).
- [42] S. J. Lin, R. J. Wu, H. Y. Tan, W. Lo, W. C. Lin, T. H. Young, C. J. Hsu, J. S. Chen, S. H. Jee, and C. Y. Dong, *Opt. Lett.* **30**, 2275–2277 (2005).
- [43] M. J. Koehler, K. Konig, P. Elsner, R. Buckle, and M. Kaatz, *Opt. Lett.* **31**, 2879–2881 (2006).
- [44] J. V. Forrester, *The Eye: Basic Sciences in Practice* (W. B. Saunders, Edinburgh, New York, 2002).
- [45] K. M. Meek, D. W. Leonard, C. J. Connon, S. Dennis, and S. Khan, *Eye* **17**, 927–936 (2003).
- [46] B. R. Masters and M. Bohnke, *Ann. Rev. Biomed. Eng.* **4**, 69–91 (2002).
- [47] S. W. Teng, H. Y. Tan, J. L. Peng, H. H. Lin, K. H. Kim, W. Lo, Y. Sun, W. C. Lin, S. J. Lin, S. H. Jee, P. T. So, and C. Y. Dong, *Investigative Ophthalmol. Vis. Sci.* **47**, 1216–1224 (2006).
- [48] W. Lo, S. W. Teng, H. Y. Tan, K. H. Kim, H. C. Chen, H. S. Lee, Y. F. Chen, P. T. C. So, and C. Y. Dong, *Microsc. Res. Tech.* **69**, 973–975 (2006).
- [49] H. Y. Tan, Y. Sun, W. Lo, S. W. Teng, R. J. Wu, S. H. Jee, W. C. Lin, C. H. Hsiao, H. C. Lin, Y. F. Chen, D. H. Ma, S. C. Huang, S. J. Lin, and C. Y. Dong, *J. Biomed. Opt.* **12**, 024013 (2007).
- [50] H. Y. Tan, Y. Sun, W. Lo, S. J. Lin, C. H. Hsiao, Y. F. Chen, S. C. Huang, W. C. Lin, S. H. Jee, H. S. Yu, and C. Y. Dong, *Investigative Ophthalmol. Vis. Sci.* **47**, 5251–5259 (2006).
- [51] N. Morishige, A. J. Wahlert, M. C. Kenney, D. J. Brown, K. Kawamoto, T. Chikama, T. Nishida, and J. V. Jester, *Investigative Ophthalmol. Vis. Sci.* **48**, 1087–1094 (2007).
- [52] S. W. Teng, H. Y. Tan, Y. Sun, S. J. Lin, W. Lo, C. M. Hsueh, C. H. Hsiao, W. C. Lin, S. C. Huang, and C. Y. Dong, *Arch. Ophthalmol.* **125**, 977–978 (2007).
- [53] D. J. Brown, N. Morishige, A. Neekhra, D. S. Minckler, and J. V. Jester, *J. Biomed. Opt.* **12**, 024029 (2007).
- [54] M. Farid, N. Morishige, L. Lam, A. Wahlert, R. F. Steinert, and J. V. Jester, *Investigative Ophthalmol. Vis. Sci.* **49**, 4377–4383 (2008).
- [55] T. T. Le, I. M. Langohr, M. J. Locker, M. Sturek, and J. X. Cheng, *J. Biomed. Opt.* **12**, 054007 (2007).
- [56] K. Schenke-Layland, J. Xie, E. Angelis, B. Starcher, K. Wu, I. Riemann, W. R. MacLellan, and S. F. Hamm-Alvarez, *Matrix Biol.* **27**, 53–66 (2008).
- [57] T. Theodossiou, G. S. Rapti, V. Hovhannisyann, E. Georgiou, K. Politopoulos, and D. Yova, *Lasers Med. Sci.* **17**, 34–41 (2002).
- [58] S. J. Lin, C. Y. Hsiao, Y. Sun, W. Lo, W. C. Lin, G. J. Jan, S. H. Jee, and C. Y. Dong, *Opt. Lett.* **30**, 622–624 (2005).
- [59] Y. Sun, W. L. Chen, S. J. Lin, S. H. Jee, Y. F. Chen, L. C. Lin, P. T. So, and C. Y. Dong, *Biophys. J.* **91**, 2620–2625 (2006).
- [60] S. J. Lin, W. Lo, H. Y. Tan, J. Y. Chan, W. L. Chen, S. H. Wang, Y. Sun, W. C. Lin, J. S. Chen, C. J. Hsu, J. W. Tjiu, H. S. Yu, S. H. Jee, and C. Y. Dong, *J. Biomed. Opt.* **11**, 034020 (2006).
- [61] M. G. Lin, T. L. Yang, C. T. Chiang, H. C. Kao, J. N. Lee, W. Lo, S. H. Jee, Y. F. Chen, C. Y. Dong, and S. J. Lin, *J. Biomed. Opt.* **11**, 064006 (2006).
- [62] H. Y. Tan, S. W. Teng, W. Lo, W. C. Lin, S. J. Lin, S. H. Jee, and C. Y. Dong, *J. Biomed. Opt.* **10**, 054019 (2005).
- [63] P. Matteini, F. Ratto, F. Rossi, R. Cicchi, C. Stringari, D. Kapsoakalyvas, F. S. Pavone, and R. Pini, *Opt. Express* **17**, 4868–4878 (2009).
- [64] T. J. Wang, W. Lo, C. M. Hsueh, M. S. Hsieh, C. Y. Dong, and F. R. Hu, *J. Biomed. Opt.* **13**, 034019 (2008).
- [65] M. Strupler, A. M. Pena, M. Herness, P. L. Tharaux, J. L. Martin, E. Beaurepaire, and M. C. Schanne-Klein, *Opt. Express* **15**, 4054–4065 (2007).
- [66] C. C. Wang, C. C. Li, R. J. Wu, V. Hovhannisyann, W. C. Lin, S. J. Lin, and C. Y. Dong, *J. Biomed. Opt.*, in press.
- [67] W. X. Sun, S. Chang, D. C. S. Tai, N. Tan, G. F. Xiao, H. H. Tang, and H. Yu, *J. Biomed. Opt.* **13**, 0064010 (2008).
- [68] T. L. Sun, Y. Liu, and Y. Sung, *J. Biomed. Opt.*, submitted.
- [69] K. M. Reiser, C. Bratton, D. R. Yankelevich, A. Knoesen, I. Rocha-Mendoza, and J. Lotz, *J. Biomed. Opt.* **12**, 064019 (2007).
- [70] M. Wang, K. M. Reiser, and A. Knoesen, *J. Opt. Soc. Am. A* **24**, 3573–3586 (2007).
- [71] S. V. Plotnikov, A. Kenny, S. Walsh, B. Zubrowski, C. Joseph, V. L. Scranton, G. A. Kuchel, D. Dauser, M. Xu, C. Pilbeam, D. Adams, R. Dougherty, P. J. Campagnola, and W. A. Mohler, *J. Biomed. Opt.* **13**, 044018 (2008).
- [72] R. Cicchi, D. Massi, S. Sestini, P. Carli, V. De Giorgi, T. Lotti, and F. S. Pavone, *Opt. Express* **15**, 10135–10148 (2007).
- [73] R. Cicchi, S. Sestini, V. De Giorgi, D. Massi, T. Lotti, and F. S. Pavone, *J. Biophoton.* **1**, 62–73 (2008).
- [74] P. P. Provenzano, D. R. Inman, K. W. Eliceiri, J. G. Knittel, L. Yan, C. T. Rueden, J. G. White, and P. J. Keely, *BMC Med.* **6**, 11 (2008).
- [75] P. P. Provenzano, K. W. Eliceiri, J. M. Campbell, D. R. Inman, J. G. White, and P. J. Keely, *BMC Med.* **4**, 38 (2006).
- [76] E. Sahai, J. Wyckoff, U. Philippar, J. E. Segall, F. Gertler, and J. Condeelis, *BMC Biotechnol.* **5**, 14 (2005).
- [77] G. Sobel, I. Szabo, C. Paska, A. Kiss, I. Kovalszky, A. Kadar, F. Paulin, and Z. Schaff, *Pathol. Oncol. Res.* **11**, 26–31 (2005).
- [78] G. R. Cunha, S. W. Hayward, and Y. Z. Wang, *Differentiation* **70**, 473–485 (2002).
- [79] R. D. Blumenthal, H. J. Hansen, and D. M. Goldenberg, *Cancer Res.* **65**, 8809–8817 (2005).
- [80] E. Brown, T. McKee, E. diTomaso, A. Pluen, B. Seed, Y. Boucher, and R. K. Jain, *Nat. Med.* **9**, 796–800 (2003).
- [81] M. E. Llewellyn, R. P. Barretto, M. J. Schnitzer, and S. L. Delp, *Proc. Am. Soc. Biomech.*, 2007.
- [82] M. E. Llewellyn, R. P. Barretto, S. L. Delp, and M. J. Schnitzer, *Nature* **454**, 784–788 (2008).
- [83] V. V. Tuchin, *J. Phys. D, Appl. Phys.* **38**, 2497–2518 (2005).
- [84] R. Cicchi, F. S. Pavone, D. Massi, and D. D. Sampson, *Opt. Express* **13**, 2337–2344 (2005).
- [85] S. Plotnikov, V. Juneja, A. B. Isaacson, W. A. Mohler, and P. J. Campagnola, *Biophys. J.* **90**, 328–339 (2006).
- [86] A. J. Wright, S. P. Poland, J. M. Girkin, C. W. Freudiger, C. L. Evans, and X. S. Xie, *Opt. Express* **15**, 18209–18219 (2007).
- [87] M. Rueckel, J. A. Mack-Bucher, and W. Denk, *Proc. Natl. Acad. Sci. USA* **103**, 17137–17142 (2006).